Engineering oxygen vacancies and surface chemical reconstruction of MOF-derived hierarchical CoO/Ni_2P-Co_2P nanosheet arrays for advanced aqueous zinc-ion batteries

Zhihao Li,[a] Qiang Jiao,[a] Shu-ang He,[a] Guanjie He,[d] Ze Cen,[c] Fang Yang,[c] Rujia Zou,[a] and Kaibing Xu*[ab]

[a] State Key Laboratory for Modification of Chemical Fibers and Polymer Materials, College of Materials Science and Engineering, Donghua University, Shanghai, 201620, China

[b] Research Center for Analysis and Measurement, Donghua University, Shanghai, 201620, China

[c] College of Mechanical and Automotive Engineering, Shanghai University of Engineering Science, Shanghai, 201620, China

[d] School of Chemistry, University of Lincoln, Brayford Pool, Lincoln LN6 7TS, UK

Email: xukaibing@dhu.edu.cn.

Abstract

Aqueous zinc-ion batteries (ZIBs) are emerging as promising alternatives among various energy storage devices. However, the lack of the research on cathode materials with both high capacity and electrochemical stability restricts the widespread applications of ZIBs. Herein, surface chemical reconstruction and partial phosphorization strategies are employed to synthesize MOF-derived hierarchical CoO/Ni_2P-Co_2P nanosheet arrays on Ni foam substrates as the cathode for ZIBs. The

unique hierarchical nanostructure and multi-component with exposed surfaces and rich oxygen vacancies accelerate the charge transfer and ion diffusion, expose more active sites, promote the accessibility between active materials and electrolyte. The oxide/phosphides composites obtained by novel partial phosphorization achieve a common improvement of performance and stability. As expected, the CoO/Ni_2P-Co_2P electrode delivers a high specific capacity (370.4 mA h g^{-1} at 3 A g^{-1}) and excellent rate performance (63.3% retention after a six-fold increase in the current density). Moreover, when employed as the cathode of CoO/Ni_2P-Co_2P-30//Zn battery, the assembled battery exhibits a superior specific capacity (322.8 mA h g^{-1} at 2 A g^{-1}), a long cycle life (104.9% retention after 6000 cycles), together with a favorable energy density (547.5 W h kg^{-1}) and a power density (9.7 kW kg^{-1}). Therefore, this study provides a suitable candidate which meets the requirements of high-performance cathode materials for ZIBs.

Keywords: Zinc-ion batteries; CoO/Ni_2P-Co_2P nanosheet arrays; Oxygen vacancies; Heterointerfaces; Partial phosphorization

1. Introduction

The threats of fossil fuel depletion and worsening environment are looming on the horizon. In this case, the research of energy storage devices has become a critical subject as we are facing up to a situation in which the demand for efficient and safe energy is ever growing. Among various devices, lithium-ion batteries (LIBs) as a representative has been developed and utilized commercially, attributed to its unique high energy density.[1, 2] However, there are several key limiting factors such as safety

issues, low power density and high cost hindering their widespread applications.[3-5] Considering these drawbacks, rechargeable aqueous batteries have attracted tremendous interests due to the fact that the aqueous electrolyte is nonflammable and cost effective.[6, 7] In addition, the water-based system provides high ionic conductivity for the enhancement of the rate performance.[8-11] Particularly, alkaline ZIBs featured with high output voltage (≈1.8 V) and high theoretical capacity of Zn anodes (≈820 mA h g^{-1}) are of great competitiveness in next-generation energy storage devices.[12, 13] However, the large-scale practical applications of ZIBs are still far from expectation owing to the insufficient research on proper cathode materials which has become a main bottleneck.[14, 15] To address this limitation, great efforts are exerted to explore different types of cathode materials with excellent electrochemical properties.

Among various cathode materials of alkaline ZIBs, transition metal oxides, including NiO[16], Co_3O_4[17], $NiCo_2O_4$[18], have been widely investigated and utilized due to their relatively high redox activity and structural stability. Particularly, transition metal oxides which are often crafted with three-dimensional structures, are commonly used as cathode materials for ZIBs because of their sufficient specific surface area and high theoretical capacitance. However, they suffer from limited kinetics during redox reactions due to their low intrinsic conductivity.[19, 20] To further extend the electrochemical performance of transition metal oxides, transition metal phosphide materials are investigated and show promise to overcome such shortcomings. Phosphorous is featured with lower electronegativity than oxygen. In this case,

phosphides and P-doped oxides show enriched density of state near the Fermi level and metalloid properties due to the lower metal-phosphorous bond strength, thereby weakening the active energy of redox reactions.[14, 21-23] They are proved to have enhanced electrical conductivity and redox activity. For example, Chen *et al* synthesized a sea-urchin-like Ni-Co-P/PO_x material by a low temperature phosphating method, which shows a specific capacity of 179.7 mA h g^{-1} at 1 A g^{-1} and a capacity retention of 67% after the current density increases by 50 times.[24] Wen et al fabricated highly conductive Ni_2P nanosheets on carbon fibers by facile phosphating process, the Ni_2P nanosheet arrays show a capacity of 242 mA h g^{-1} at 1 A g^{-1}.[25] Despite the recent progress, transition metal phosphides still suffer from relatively low rate capability arising from the fact that phosphides are difficult at sustainably resisting the corrosive effects of alkaline electrolyte and maintain structural integrity.[26, 27] Compared with transition metal phosphides, oxides are often considered to have a more stable structural stability to resist the electrolyte corrosion and collapse during cycling.[28-31] Conceivably, combining transition metal phosphides and oxides together can be imagined as a better way to improve the overall electrochemical performance. To the best of our knowledge, the partial phosphorization method was rarely used to design an oxide/phosphides composites structure. By this way, transition metal oxides are reduced to lower valence state metal oxides, transition metal phosphides are formed and oxygen vacancies are introduced into the host materials to induce an electron redistribution. The electrons in vacancies can be stimulated into the conduction band to create a new gap in the conduction band that is favorable for promoting the transferring of charge carriers.[32-34]

Also, heterointerfaces between different components of oxides and phosphides serve as fast channel for ion diffusion and charge transfer. Therefore, constructing hierarchical nanoarchitecture based on transition metal oxides/phosphides composites with abundant active sites and rich oxygen vacancies would be a feasible way to facilitate the intrinsic conductivity, reaction kinetics and electrochemical stability of ZIBs.

Based on the above considerations, herein, MOF-derived hierarchical CoO/Ni_2P-Co_2P nanosheet arrays on Ni foam are synthesized by surface chemical reconstruction and phosphating treatment for ZIBs. The electrochemical performance of as-prepared CoO/Ni_2P-Co_2P was significantly extended by synergistic effects of oxygen vacancies and hierarchical architecture. The optimized CoO/Ni_2P-Co_2P electrode delivers the highest capacity of 370.4 mA h g^{-1} at 3 A g^{-1}, and 63.3% of its initial value is achieved after a six-fold increase of the current density. When assembled into a CoO/Ni_2P-Co_2P-30//Zn battery, the device exhibits the highest capacity of 322.8 mA h g^{-1} at 2 A g^{-1}, together with a maximum energy density of 547.5 W h kg^{-1} at a power density of 3.4 kW kg^{-1}.

2. Experimental

2.1. Preparation of Co-MOF and NiCo-LDH/$Co(OH)_2$ nanosheet arrays on Ni foam

All chemicals are of analytical-reagents and used without any further treatment. The cobalt-based metal-organic frameworks (Co-MOF) were directly grown on Ni foam

under an aqueous reaction condition. Firstly, 2-methylimidazole (2-MIM) (0.4 M, 40 mL) aqueous solution and $Co(NO_3)_2 \cdot 6H_2O$ (0.05 M, 40 mL) aqueous solution were prepared respectively, then the former was quickly poured into the latter followed by vigorous stirring for 1 minute. Subsequently, a piece of pre-cleaned Ni foam (1×4 cm^2) was immersed into the solution for 4 h under ambient conditions. After that, the as-obtained sample was washed by deionized water and then dried in vacuum at 60 °C overnight to obtain Co-MOF nanosheet arrays on Ni foam. The as-obtained sample was then immersed into $Ni(NO_3)_2 \cdot 6H_2O$ (0.014 M, 40 mL) aqueous solution and remained stationary for 90 minutes (30, 60 and 120 minutes for comparison). Finally, the product was taken out, washed by deionized water and dried in vacuum at 60 °C overnight to obtain NiCo-LDH/$Co(OH)_2$ nanosheet arrays on Ni foam.

2.2. Preparation of $NiCo_2O_4$/NiO and CoO/Ni_2P-Co_2P nanosheet arrays on Ni foam

To obtain $NiCo_2O_4$/NiO, the above-prepared NiCo-LDH/$Co(OH)_2$ nanosheet arrays on Ni foam were calcinated in air at 300 °C for 2 h. Subsequently, the as-obtained $NiCo_2O_4$/NiO and 0.3 g of NaH_2PO_2 were placed in two separated ceramic boats in a furnace with the NaH_2PO_2 at the upstream of the gas flow. Then the center of the furnace was heated up to 300 °C at a rate of 2 °C min^{-1} in N_2 atmosphere, the phosphating treatment was kept for 15, 30, 60, and 120 minutes, and the products denoted as CoO/Ni_2P-Co_2P-15, 30, 60, 120, respectively. The mass loading of CoO/Ni_2P-Co_2P on the Ni foam was 1.0-1.2 mg cm^{-2}.

2.3. Characterization

The morphologies and microstructures of the samples were observed and analyzed by a scanning electron microscope (SEM; Hitachi, S-4800), a transmission electron microscope (TEM; FEI, Talos F200S). The phase compositions and elemental valence states analysis were conducted on an X-ray diffractometer (XRD; Rigaku, D/max-2550 PC) and an X-ray photoelectron spectrometer (XPS; Thermal Fisher, Escalab 250Xi). The specific surface area of the sample was measured on a Brunauer-Emmett-Teller analyzer (BET; Quantachrome, Autosorb-iQ). Electron paramagnetic resonance (EPR; Bruker, A300-10/12) was used to investigate the electron structure.

2.4. Electrochemical Measurement

The electrochemical measurements were performed on an Autolab electrochemical workstation (PGSTAT302N, Utrecht, The Netherlands). Cyclic Voltammetry (CV), galvanostatic charge/discharge (GCD) measurements and electrochemical impedance spectroscopy (EIS) were carried out based on a three-electrode configuration with 1 × 1 cm^2 of the as-prepared materials as the working electrode, a saturated calomel electrode (SCE) as the reference electrode and a platinum foil (Pt) as the counter electrode in a 1 M KOH solution.

As for the assembly of CoO/Ni_2P-Co_2P//Zn and $NiCo_2O_4$/NiO//Zn batteries, 1 × 1 cm^2 of CoO/Ni_2P-Co_2P and $NiCo_2O_4$/NiO were employed as cathode materials respectively, 1 × 1 cm^2 of a commercial zinc plate was employed as the anode, a mixed solution of 1 M KOH and 0.01 M $Zn(CH_3COO)_2$ was employed as the electrolyte.

2.5. Calculation Principles

For the calculations of the electrodes' specific capacity (mA h g^{-1}), the following equation was applied:

$$C = \frac{i\,\Delta t}{m} \tag{1}$$

Where C is the specific capacity (mA h g^{-1}), i (mA) is the applied discharge current, Δt (h) is the discharge time and m (g) is the mass loading of the active materials.

The energy density E (W h kg^{-1}) and power density P (W kg^{-1}) are estimated based on the following formulas:

$$E = \int_0^{\Delta t} \frac{V\,i}{m}\,dt \tag{2}$$

$$P = \frac{E}{t} \tag{3}$$

In which V (V), i (mA), Δt (h) and m (g) represent the working voltage, discharge current and discharge time of the assembled batteries, mass loading of the active materials, respectively.

3. Results & discussion

The detailed fabrication process of MOF-derived hierarchical CoO/Ni_2P-Co_2P nanosheet arrays is schematically demonstrated in Fig. 1. Firstly, well-defined Co-MOF nanosheet arrays directly grown on Ni foam substrate are facilely obtained by a room-temperature solution deposition route.[35] Then the substrate is immersed into a $Ni(NO_3)_2$

solution and keeps stationary. During this process, Ni^{2+} undergoes a hydrolysis process to produce $Ni(OH)_2$ and H^+ reversibly, and thus H^+ begins to react with 2-MIM linkers to continuously etch the Co-MOF and form a deposition layer from the outermost to the inner position. Subsequently, the etched samples are calcinated to obtain $NiCo_2O_4$/NiO nanosheet arrays, and are further annealed in N_2 atmosphere at 300 °C for 0.5 h with the presence of NaH_2PO_2, resulting in the oxygen vacancies and surface chemical reconstruction of CoO/Ni_2P-Co_2P nanosheet arrays. The as-prepared CoO/Ni_2P-Co_2P shows great advantages in cathode materials for ZIBs, mainly attributed to the following reasons: (i) The hierarchical nanosheets architecture and heterointerfaces between different components provide rich electroactive surface area and fast ion diffusion channels respectively for boosting redox reactions kinetics. (ii) The introduced oxygen vacancies provide extra charges for improving its intrinsic electrical conductivity, resulting in the improvement of the electrochemical performances. (iii) The combination of metallic transition metal phosphides and stable oxides contributes to electrical conductivity enhancement and structural integrity synergistically.

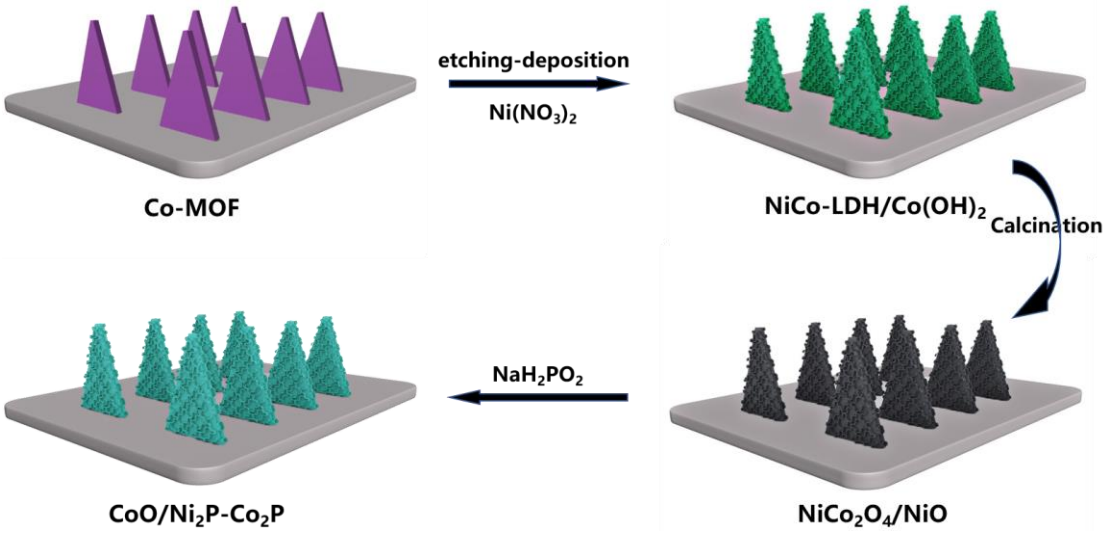

Fig. 1 Schematic of the synthesis route of the CoO/Ni_2P-Co_2P nanosheet arrays supported on the Ni foam substrate.

As reflected by the scanning electron microscope (SEM) images in Fig. 2a, the surface of Ni foam is uniformly covered with Co-MOF nanosheets, and these nanosheet arrays can serve as templates for etching and deposition of nickel and cobalt hydroxides. Fig. S1 shows the typical morphologies of Co-MOF after the transformation in the presence of $Ni(NO_3)_2$ with different etching time. It can be clearly seen that more and more substantial small-size metal hydroxides nanosheets growing on the surface of Co-MOF with the increase of etching time. Obviously, the overall array structures could be well preserved after the in-situ transformation, showing good structural stability. In more detail, the electrochemical performances of these samples after subsequent phosphorization are tested and shown in Fig. S2 and Fig. S3. The sample etched for 90 minutes is proved to have the highest specific capacity. Fig. 2b and c show the SEM images of the $NiCo_2O_4/NiO$ nanosheet arrays. It is worth noting that the morphology of the nanosheets was well preserved after the subsequent calcination process.

Subsequently, transmission electron microscopy (TEM) was employed to investigate the microstructures of $NiCo_2O_4$/NiO sample in detail. From the TEM image in Fig. 2d, dense nanosheets can be clearly seen on the single $NiCo_2O_4$/NiO nanosheet. And from the high-resolution TEM (HRTEM) image in Fig. 2e, lattice fringes with interlayer distances of 0.245 nm and 0.209 nm are detected, which correspond well to the (311) lattice plane of $NiCo_2O_4$ and (200) lattice plane of NiO respectively. Moreover, EDS elemental mapping (Fig. 2f) conducted on the single $NiCo_2O_4$/NiO nanosheet demonstrates that Ni, Co and O elements are uniformly distributing throughout the array. These results confirm the $NiCo_2O_4$/NiO composites structure obtained after the calcination in air.

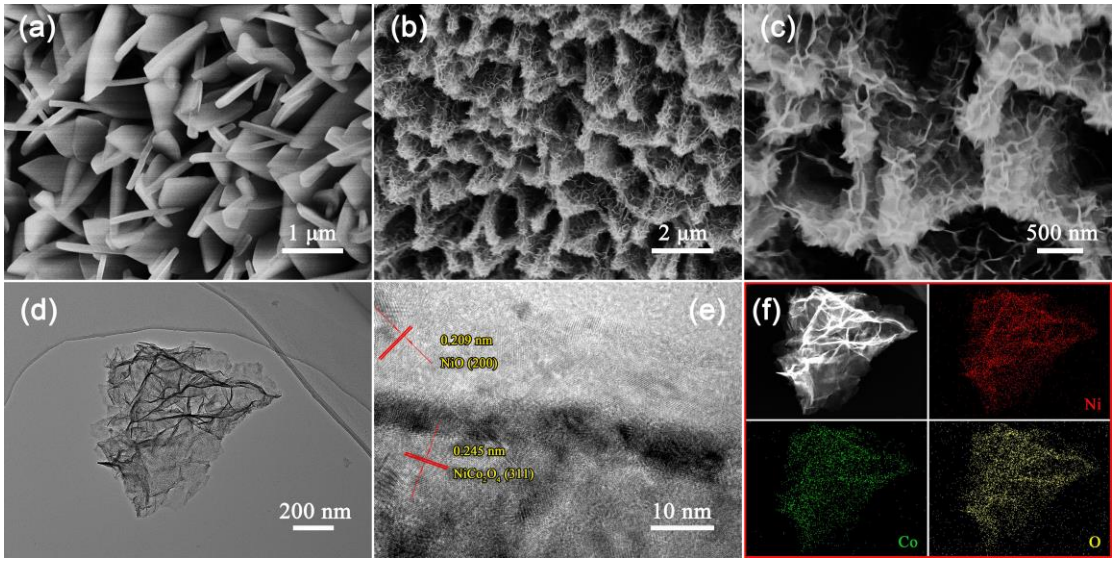

Fig. 2 (a) SEM image of Co-MOF nanosheet arrays; (b, c) SEM images, (d) TEM image, (e) HRTEM image and (f) corresponding EDS elemental mapping images of $NiCo_2O_4$/NiO nanosheet arrays.

As shown in Fig. 3a, the typical SEM image of CoO/Ni_2P-Co_2P indicates that the array structure is still well preserved during phosphorization process. Such hierarchical nanosheets substantially promote the ion diffusion and charge transfer with more electrochemically active sites exposed. As for the TEM image of CoO/Ni_2P-Co_2P nanosheet in Fig. 3b, it can be clearly observed that abundant nanoparticles are created and embedded in the nanosheets. These nanoparticles can be assigned to Co_2P or Ni_2P nanoparticles generated from the breaking of the Co (or Ni)-O bond under the PH_3 vapor environment. These newly formed nanoparticles can serve as active sites for fast redox reactions to improve electrochemical performance. As exhibited in Fig. S4, the BET specific surface area of CoO/Ni_2P-Co_2P sample was obtained by the nitrogen adsorption/desorption isotherms test. CoO/Ni_2P-Co_2P with a large specific surface area of 38.1 $m^2 g^{-1}$ demonstrates the sufficient active surface area for the occurrence of redox reactions. The HRTEM image in Fig. 3c shows the lattice spacing of 0.246 nm, 0.209 nm and 0.221 nm, which correspond well to the (111) lattice plane of CoO, (210) lattice plane of Ni_2P and (121) lattice plane of Co_2P, respectively. Moreover, the EDS analysis (Fig. 3d) and elemental mapping image (Fig. 3e) obtained from the CoO/Ni_2P-Co_2P nanosheet verifies the existence and homogeneous distribution of Ni, Co, O and P elements.

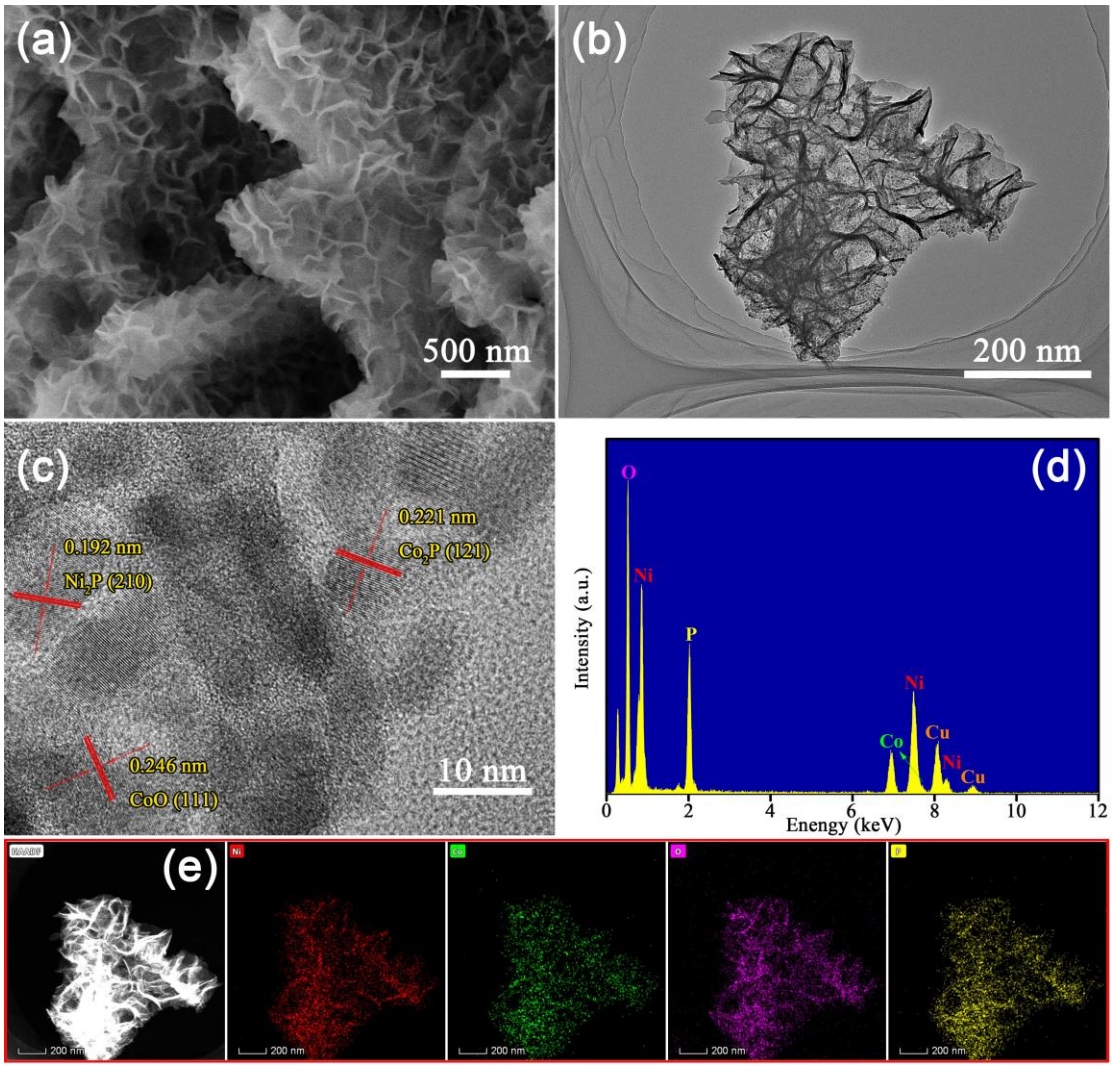

Fig. 3 (a) SEM image, (b) TEM image, (c) HRTEM image, (d) EDS analysis and (e) corresponding EDS elemental image of CoO/Ni_2P-Co_2P sample.

X-ray diffraction (XRD) was adopted to further investigate the conversion of phase compositions during the fabrication process. The XRD patterns of Co-MOF and metal hydroxides are depicted in Fig. S5. For Co-MOF, the locations of peaks are consistent with that of the reported literatures, which verifies the successful preparation of Co-MOF. For the as-made metal hydroxides, the peaks at 11.0°, 21.9°, 34.1°, 38.5°, 43.9° and 60.3° can be indexed to (003), (006), (012), (015), (018) and (110) lattice planes of

hydrotalcite-like structure NiCo-LDH.[36-38] And the remaining peaks correspond well to the characteristic peaks of $Co(OH)_2$ (JCPDS: 02-0925). Thus it can be inferred that the metal hydroxides is composed of hydrotalcite-like structure NiCo-LDH and $Co(OH)_2$. As reflected clearly by the XRD pattern of CoO/Ni_2P-Co_2P sample (Fig. 4a), the diffraction peaks locate at 30.9°, 41.0°, 51.7° and 75.3° can be indexed to (120), (201), (131) and (312) lattice planes of Co_2P (JCPDS: 32-0306), respectively. The diffraction peaks locate at 40.8°, 44.5°, 47.4°, 54.8 and 74.9° can be indexed to (111), (201), (210), (211) and (400) lattice planes of Ni_2P (JCPDS: 03-0953), respectively. And the diffraction peaks locate at 36.4°, 42.4° and 61.8° can be indexed to (111), (200) and (220) lattice planes of CoO (JCPDS: 43-1004), respectively. As for the XRD pattern of $NiCo_2O_4$/NiO sample (Fig. 4b), the diffraction peaks locate at 31.1°, 36.7°, 55.3°, 59.2° and 65.0° are attributed to (220), (311), (422), (511) and (440) lattice planes of $NiCo_2O_4$ (JCPDS: 20-0781), respectively, and the diffraction peaks locate at 42.9°, 62.7° and 75.3° are attributed to (200), (220) and (311) lattice planes of NiO (JCPDS: 47-1049), respectively.

Moreover, X-ray photoelectron spectroscopy (XPS) was used to research the evolution of elemental valences of such two samples. As shown in the survey spectra in Fig. 4c, the peaks attributed to Ni, Co and O can be identified in both patterns, and the appearance of P signal strongly indicates the co-existence of P with Ni, Co and O in CoO/Ni_2P-Co_2P sample. Further evidenced by the P 2p core-level spectra in Fig. 4d, two peaks locate at 129.6 eV and 130.5 eV can be assigned to the P element existing in

Co-P and Ni-P bonds. And a dominant peak centering at 134.2 eV represents the diagnostic peak of phosphate species. In the Co 2p region of $NiCo_2O_4$/NiO (Fig. 4e), two peaks at 797.0 eV and 781.4 eV are ascribed to Co $2p_{1/2}$ and Co $2p_{3/2}$ of Co^{2+}, and the binding energies at 795.0 eV and 779.5 eV are ascribed to Co^{3+} with obvious shakeup satellites at around 802.9 eV and 787.0 eV. As for the Co 2p spectra of CoO/Ni_2P-Co_2P, Co^{2+} can be deconvoluted into two peaks at 782.0 eV and 798.1 eV with two satellite peaks at 786.5 eV and 803.0 eV. And the binding energies at 778.5 eV and 793.3 eV might be ascribed to the Co-P bond originating from Co_2P, such results can also be observed in other CoP-based materials.[39, 40] The above-mentioned reasons indicate the co-existence of CoO and Co_2P due to the partial phosphating. In Fig. 4f, one can see the Ni 2p spectra is similar to Co 2p spectra of both samples. For $NiCo_2O_4$/NiO, two peaks at 871.4 eV and 854.0 eV are ascribed to Ni $2p_{1/2}$ and Ni $2p_{3/2}$ of Ni^{3+}, and the binding energies at 873.1 eV and 855.7 eV are ascribed to Ni^{2+} with obvious shakeup satellites at around 879.2 eV and 861.2 eV. As for CoO/Ni_2P-Co_2P, it should be noted that the peaks at 874.8 eV and 856.9 eV could be assigned to the partial oxidation of Ni species with two satellite peaks at 880.3 eV and 861.9 eV. Importantly, the peaks at 870.6 eV and 853.2 eV can be assigned to $Ni^{\delta+}$ in Ni-P species. Evidently, after the phosphating treatment, the Ni species in $NiCo_2O_4$ were converted into $Ni^{\delta+}$ in Ni_2P.[32] In the O 1s spectra (Fig. 4g) of $NiCo_2O_4$/NiO, the fitted peaks at 532.4 eV, 531.1 eV and 529.4 eV correspond to absorbed water (O-H), oxygen vacancies with a low oxygen coordination and metal-oxygen bonds, respectively. For CoO/Ni_2P-Co_2P, the intensity of metal-oxygen bonds was extremely weakened due to the formation of

metal-phosphorous bonds and the increase of oxygen vacancies.[41] Furthermore, electron paramagnetic resonance (EPR) was employed to explore the influence of phosphating treatment on the coordination of oxygen atoms. As shown in Fig. 4h, one can see that the peak intensity at about g = 2.0 of CoO/Ni_2P-Co_2P is much higher than that of $NiCo_2O_4$/NiO, indicating the increased number of oxygen vacancies and unpaired electrons, which accounts for the increase of lower valence states of Ni and Co elements. Specifically, oxygen vacancies introduced by phosphating treatment serve as extra active sites for enhancing the reaction kinetics, and modulate the electron structures to improve the intrinsic conductivity.

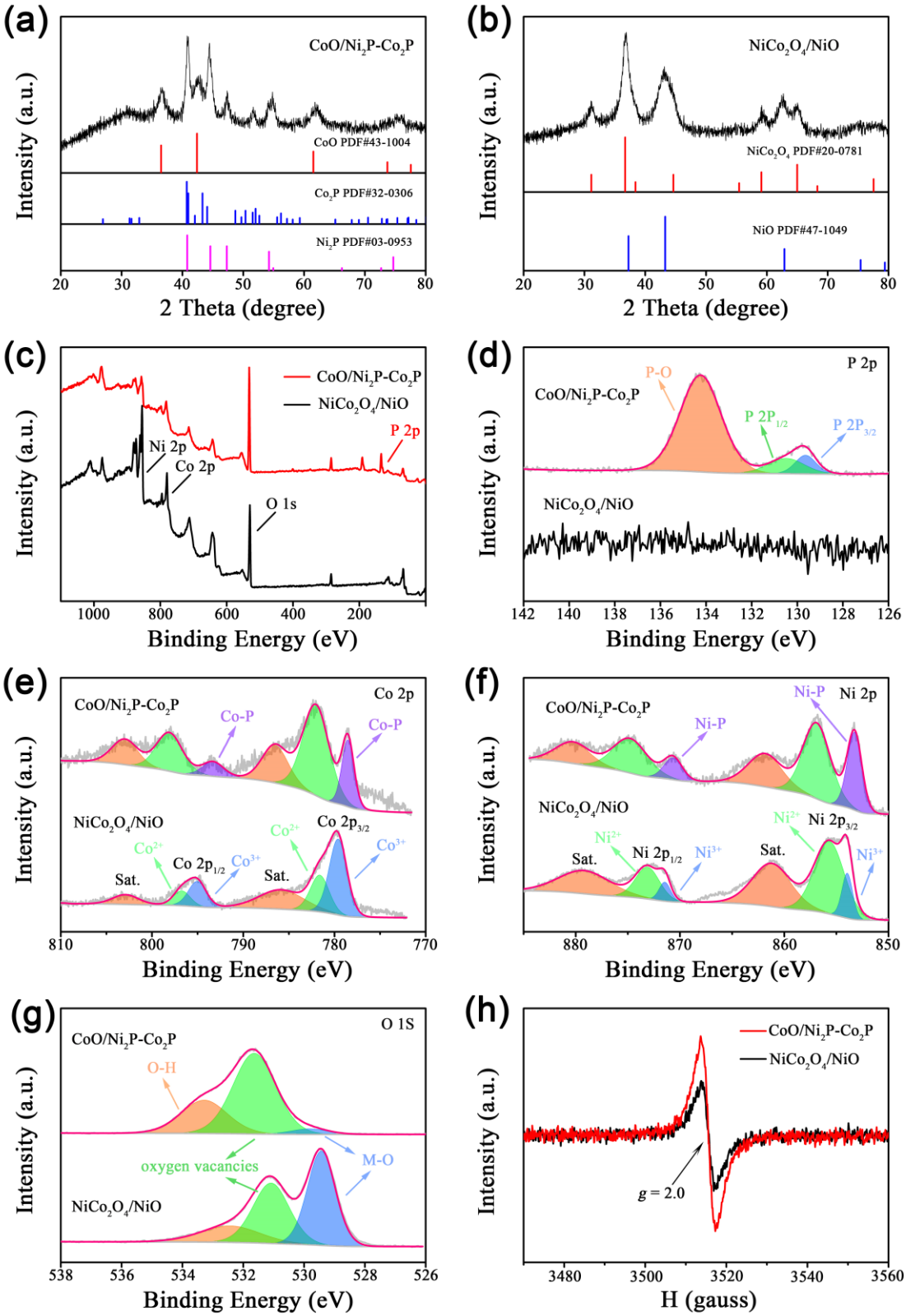

Fig. 4 XRD patterns of (a) CoO/Ni2P-Co2P sample and (b) NiCo2O4/NiO sample, (c) XPS survey spectra of CoO/Ni2P-Co2P sample and NiCo2O4/NiO sample, (d) P 2p, (e) Co 2p, (f) Ni 2p, (g) O 1s high resolution XPS spectra of CoO/Ni2P-Co2P sample and

$NiCo_2O_4$/NiO sample, (h) EPR spectra of CoO/Ni_2P-Co_2P sample and $NiCo_2O_4$/NiO sample.

The electrochemical properties of these electrodes are demonstrated in a three-electrode configuration in 1 M KOH electrolyte. The cyclic voltammetry (CV) curves of CoO/Ni_2P-Co_2P and $NiCo_2O_4$/NiO electrode are compared at the scan rate of 10 mV s^{-1} as shown in Fig. 5a. Obviously, the enclosed curve of CoO/Ni_2P-Co_2P electrode has much greater integrated area than the other one, indicating the enhanced specific capacity of CoO/Ni_2P-Co_2P electrode. Fig. 5b clearly displays CV curves of CoO/Ni_2P-Co_2P electrode at different scan rates from 10 to 50 mV s^{-1}. With the increase of scan rates, these CV curves show typical redox peaks, remain almost symmetric shape and notably high current densities, indicating the reversible and ultra-stable redox reactions. The CV curves of $NiCo_2O_4$/NiO electrode at various scan rates are also demonstrated in Fig. S6. Moreover, the $NiCo_2O_4$/NiO sample treated at different phosphating time of 15, 30, 60 and 120minutes were obtained, from the discharge curves (Fig. 5c) of different samples tested at the current density of 3 A g^{-1}, it was found that the specific capacity of CoO/Ni_2P-Co_2P-30 up to 370.4 mA h g^{-1} significantly exceeds those of $NiCo_2O_4$/NiO (75.0 mA h g^{-1}) and CoO/Ni_2P-Co_2P-15, 60, 120 (303.8 mA h g^{-1}, 287.1 mA h g^{-1}, 207.1 mA h g^{-1}, respectively). Fig. 5e shows the specific capacities as a function of current densities calculated based on the discharge curves (Fig. 5d and Fig. S7). The specific capacity of CoO/Ni_2P-Co_2P-30 electrode can reach up to 370.4, 300.8, 273.8, 256.7, 245.4, 234.5 mA h g^{-1} at 3, 6, 9, 12, 15, 18 A g^{-1}, respectively. Importantly,

the CoO/Ni_2P-Co_2P-30 electrode shows a capacitance retention of 63.3% when the current density increases from 3 to 18 A g^{-1}. The as-prepared CoO/Ni_2P-Co_2P-30 electrode outperforms many counterparts reported before, for example, R-Co_3O_4 nanosheets (212.6 mA h g^{-1} at 2 mA cm^{-1})[42], Co-doped $NiMoO_4$ nanosheets (361.4 mA h g^{-1} at 3 A g^{-1})[15], Co_3S_4 nanosheets (348 mA h g^{-1} at 1 A g^{-1})[43], Ni_3S_2@PANI (247.6 mA h g^{-1} at 11.4 A g^{-1})[44], sd-$NiCo_2S_{4-x}$@CC (298.3 mA h g^{-1} at 0.5 A g^{-1})[45], Ni-NiO@CC (184 mA h g^{-1} at 0.625 A g^{-1})[16]. The enhanced specific capacity of the CoO/Ni_2P-Co_2P-30 electrode is mainly attributed to the improved electrical conductivity and reaction kinetics caused by introducing oxygen vacancies and surface chemical reconstruction from the phosphating process. To further evaluate the cycling stability of CoO/Ni_2P-Co_2P-30 electrode, cycling test was conducted at 60 mV s^{-1} and the profiles were plotted in Fig. 5f. After 8000 cycles, above 88% of its initial capacity is maintained. Moreover, we compared the Nyquist plots (inserted in Fig. 5f) before and after cycling test to evaluate the overall cycling performance. It is found that the internal resistance (*Rs*) of CoO/Ni_2P-Co_2P-30 electrode before (1.4 Ω) and after (1.6 Ω) cycling remained almost unchanged. The slope in low-frequency is nearly the same, indicating the ion diffusion rate of the cycled electrode is as fast as the initial one, only with an increase in the diameter of semicircle in the high-frequency, which suggests a weakened charge transfer rate. The excellent cycling stability can be attributed to the rigid hierarchical nanosheets structure avoiding the collapse of the active materials. Theoretically, the charge storge mechanism of CoO/Ni_2P-Co_2P-30 electrode is estimated based on the relationship between peak currents (i) and the square root of scan rates ($v^{1/2}$). The linear

fitting of the relationship depicted in Fig. S8 demonstrates that the oxidation and reduction reactions are typical diffusion-controlled process.

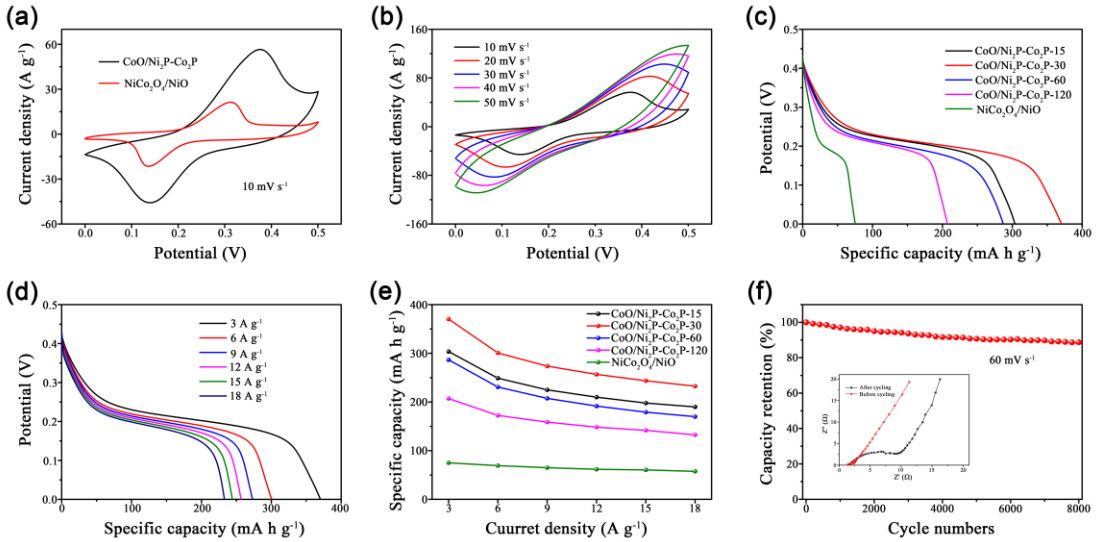

Fig. 5 (a) Comparison of CV curves for CoO/Ni_2P-Co_2P-30 electrode and $NiCo_2O_4$/NiO electrode at 10 mV s^{-1}, (b) CV curves tested at various scan rates of CoO/Ni_2P-Co_2P-30 electrode, (c) discharge curves tested at 3 A g^{-1} of $NiCo_2O_4$/NiO and CoO/Ni_2P-Co_2P electrodes treated at different phosphating time, (d) discharge curves tested at various current densities of CoO/Ni_2P-Co_2P-30 electrode, (e) comparison of specific capacities at various current densities for $NiCo_2O_4$/NiO and CoO/Ni_2P-Co_2P electrodes and (f) cycling stability of CoO/Ni_2P-Co_2P-30 electrode at 60 mV s^{-1} and the inserted Nyquist plots of it before and after cycling.

For assessing the utilization potential of our CoO/Ni_2P-Co_2P-30 cathode, a CoO/Ni_2P-Co_2P-30//Zn alkaline battery was constructed with a Zn plate as the anode, CoO/Ni_2P-Co_2P-30 as the cathode, the mixed solution of 1 M KOH and 0.01 M $Zn(CH_3COO)_2$ as

the electrolyte. The charge transfer and ion diffusion processes happen in CoO/Ni_2P-Co_2P-30//Zn battery are schematically shown in Fig. 6a. Fig. 6b displays the CV curves of CoO/Ni_2P-Co_2P-30//Zn at scan rates of 10, 20, 30, 40, 50 mV s^{-1} within a wide range of operating voltage (1.4-2.0 V). The curves remain almost symmetric shape with apparent redox peaks despite of increased scan rates, and the curves reach considerable current densities, demonstrating the highly reversible, stable and active redox reactions occurred in the battery. For comparison, the CV curves of $NiCo_2O_4$/NiO//Zn battery are displayed in Fig. S9a. For CD profiles, it can be seen in Fig. 6c that the galvanostatic charge/discharge (GCD) curves exhibit ultra-flat discharge plateaus and high Coulombic efficiency with the current densities varying from 2 to 6 A g^{-1}, and the discharge voltage located at about 1.55-1.7 V. More importantly, the CoO/Ni_2P-Co_2P-30//Zn battery delivers a satisfactory capacity of 322.8, 266.6, 186.1, 127.1, 84.2 mA h g^{-1} at a current density of 2, 3, 4, 5, 6 A g^{-1}, respectively. Moreover, the comparison of the specific capacities for CoO/Ni_2P-Co_2P-30//Zn battery and $NiCo_2O_4$/NiO//Zn (Fig. S9b) battery are depicted in Fig. 6d, the CoO/Ni_2P-Co_2P-30//Zn battery offers a three times higher capacity (322.8 mA h g^{-1}) than the latter one (103.5 mA h g^{-1}). Furthermore, we conducted the GCD measurements at a series of gradually increased current densities to exemplify the rate performance and Coulombic efficiency as shown in Fig. 6e. Notably, when cycles are performed for ten times at each current density of 2, 3, 4, 5, 6 A g^{-1}, the CoO/Ni_2P-Co_2P-30//Zn battery still achieves an average capacity of 333.5, 288.9, 210.3, 147.0, 109.9 mA h g^{-1}, respectively. Particularly, when the current density returns to 2 A g^{-1}, the capacity can still recover to an average level of 363.2 mA h g^{-1}

after 50 cycles. Notably, the Coulombic efficiency always exceeds the value of 90%. To further understand the overall cycling stability of the CoO/Ni_2P-Co_2P-30//Zn battery, cycling test was conducted at a scan rate of 30 mV s^{-1} as depicted in Fig. 6f. After 6000 cycles, about 104.9% of its initial value can be maintained.

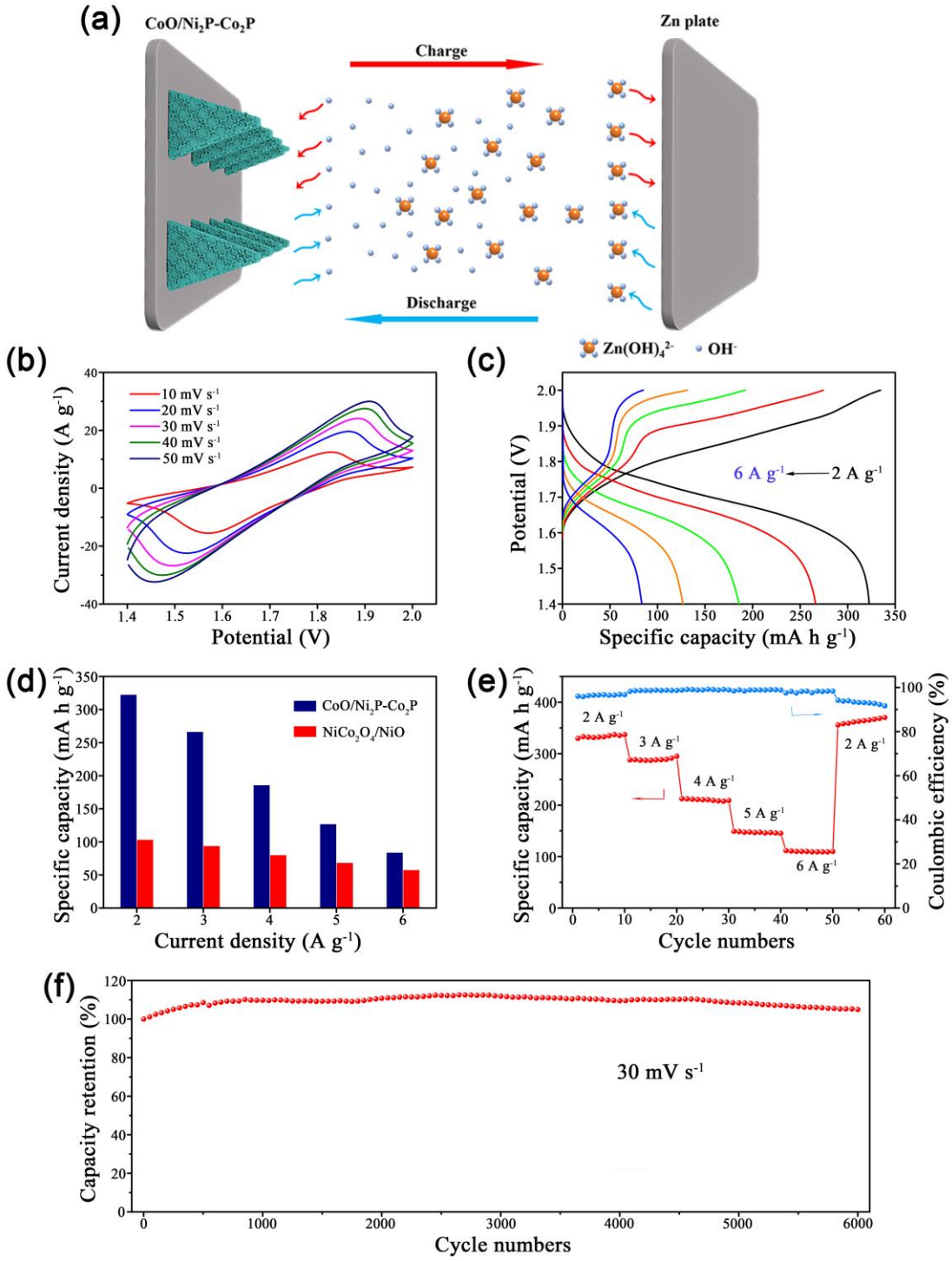

Fig. 6 (a) Schematic illustration of charge transfer and ion diffusion in CoO/Ni_2P-Co_2P-30//Zn battery, (b) CV curves at various scan rates and (c) GCD curves at various current densities of CoO/Ni_2P-Co_2P-30//Zn battery, (d) comparison of specific capacities at various current densities for CoO/Ni_2P-Co_2P-30//Zn battery and $NiCo_2O_4$/NiO//Zn battery, (e) rate performance of CoO/Ni_2P-Co_2P-30//Zn battery and (f) cycling performance of CoO/Ni_2P-Co_2P-30//Zn battery.

Energy density and power density are two critical parameters for determining the practical commercial value of energy storage devices. Noticeably, the CoO/Ni_2P-Co_2P-30//Zn battery exhibits desirable energy density and power density as evidenced in the Ragone plot of Fig. 7a. A remarkable energy density of 547.5 W h kg^{-1} is delivered based on the mass of the active materials at a power density of 3.4 kW kg^{-1}. Even though at 9.7 kW hg^{-1}, the energy density can reach up to 135.6 W h kg^{-1}. Evidently, the as-assembled battery shows fantastic electrochemical properties, surpassing many of the similar studies reported before, such as Ni/NiO-BCF//Zn (313.4 W h kg^{-1} at 0.66 kW kg^{-1})[46], R-Co_3O_4//Zn (295.5 W h kg^{-1} at 0.84 kW kg^{-1})[42], Co_3O_4@NiV-LDH//Zn (143.5 W h kg^{-1} at 1.14 kW kg^{-1})[47], NNA@CNH//NNA@Zn (148.54 W h kg^{-1} at 1.725 kW kg^{-1})[19], CCH@CMO//Zn (235 W h kg^{-1} at 1.97 kW kg^{-1})[48], HD-NiS_2/rGO-5//Zn (357.7 W h kg^{-1} at 1.75 kW kg^{-1})[49], CC/Co@NCNTs/α-$Ni(OH)_2$//Zn (540.4 W h kg^{-1} at 1.72 kW kg^{-1})[50] and NiS/$Ni_{0.95}Zn_{0.05}(OH)_2$//Zn (237 W h kg^{-1} at 5.87 kW kg^{-1})[51]. To demonstrate the practical value of our assembled devices, two as-fabricated CoO/Ni_2P-Co_2P-30//Zn batteries were connected in series which can light up seven green LEDs when charged

at a constant current of 3 mA over to 3.5 V.

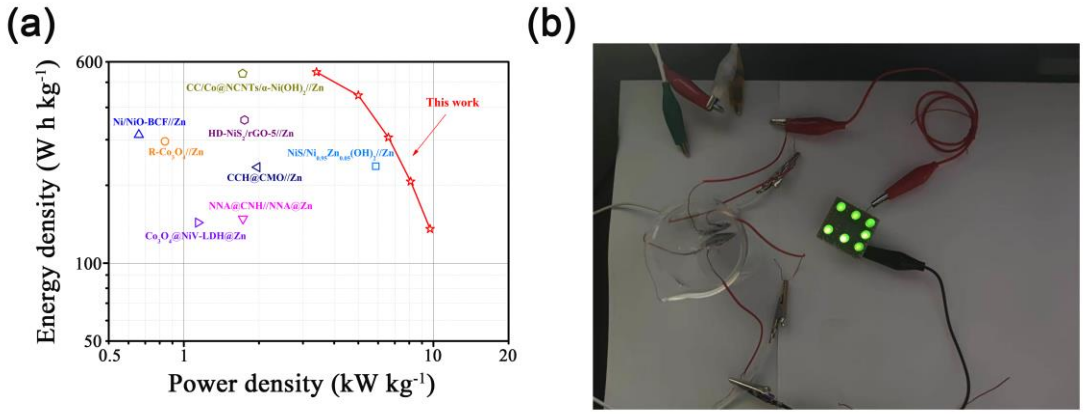

Fig. 7 (a) Ragone plot comparing the energy density and power density of CoO/Ni_2P-Co_2P-30//Zn battery with those of other devices and (b) digital photograph of two CoO/Ni_2P-Co_2P-30//Zn batteries in series powering seven LEDs.

4. Conclusions

In summary, the MOF-derived hierarchical CoO/Ni_2P-Co_2P nanosheet arrays supported on a Ni foam substrate are successfully fabricated through surface chemical reconstruction and phosphating process. The CoO/Ni_2P-Co_2P materials shows hierarchical nanoarchitecture with large specific surface area for enhancing the exposure of active materials. More importantly, rich oxygen vacancies are introduced into the active materials to modulate the electron structures, thereby enhancing its intrinsic conductivity and reaction kinetics. The heterointerfaces between transition metal phosphides and oxide composites serve as fast channel for ion diffusion and are beneficial for maintaining the structural integrity. Benefiting from these merits, favorable electrochemical performances are achieved on the CoO/Ni_2P-Co_2P electrode.

The optimized CoO/Ni_2P-Co_2P electrode delivers a high specific capacity of 370.4 mA h g^{-1} at 3 A g^{-1}, which significantly exceeds that of Co_3O_4/$NiCo_2O_4$ (75.0 mA h g^{-1}), and retains its 63.3% at a current density of 18 A g^{-1}. When assembled into the CoO/Ni_2P-Co_2P-30//Zn battery, the system exhibits an admirable specific capacity of 322.8 mA h g^{-1} at 2 A g^{-1}, superior cycling stability (104.9% retention after 6000 cycles), together with a favorable energy density (547.5 W h kg^{-1}) and a power density (9.7 kW kg^{-1}). Such exceptional performances of our CoO/Ni_2P-Co_2P make it a promising candidate for cathode materials in aqueous alkaline batteries.

Conflicts of interest

There are no conflicts to declare.

Acknowledgements

This work was financially supported by the National Natural Science Foundation of China (Grant No. 51602049) and China Postdoctoral Science Foundation (2017M610217 and 2018T110322).

References

1. Z. Zheng, H. H. Wu, H. Liu, Q. Zhang, X. He, S. Yu, V. Petrova, J. Feng, R. Kostecki, P. Liu, D. L. Peng, M. Liu and M. S. Wang, *ACS Nano*, 2020, **14**, 9545-9561.
2. R. Wang, J. Yang, X. Chen, Y. Zhao, W. Zhao, G. Qian, S. Li, Y. Xiao, H. Chen, Y. Ye, G. Zhou and F. Pan, *Adv. Energy Mater.*, 2020, **10**, 1903550.
3. H. Geng, M. Cheng, B. Wang, Y. Yang, Y. Zhang and C. C. Li, *Adv. Funct. Mater.*, 2019, **30**, 1907684.
4. C. Wang, Y. Zeng, X. Xiao, S. Wu, G. Zhong, K. Xu, Z. Wei, W. Su and X. Lu, *J. Energy Chem.*, 2020, **43**, 182-187.

5. H. Jiang, Y. Zhang, L. Xu, Z. Gao, J. Zheng, Q. Wang, C. Meng and J. Wang, *Chem. Eng. J.*, 2020, **382**, 122844.
6. Q.-N. Zhu, Z.-Y. Wang, J.-W. Wang, X.-Y. Liu, D. Yang, L.-W. Cheng, M.-Y. Tang, Y. Qin and H. Wang, *Rare Metals*, 2020, **40**, 309-328.
7. J. Wang, Y. Yang, Y. Zhang, Y. Li, R. Sun, Z. Wang and H. Wang, *Energy Storage Mater.*, 2021, **35**, 19-46.
8. M. Mao, X. Wu, Y. Hu, Q. Yuan, Y.-B. He and F. Kang, *J. Energy Chem.*, 2021, **52**, 277-283.
9. D. Chen, M. Lu, B. Wang, R. Chai, L. Li, D. Cai, H. Yang, B. Liu, Y. Zhang and W. Han, *Energy Storage Mater.*, 2021, **35**, 679-686.
10. Z. Zhao, J. Zhao, Z. Hu, J. Li, J. Li, Y. Zhang, C. Wang and G. Cui, *Energy Environ. Sci.*, 2019, **12**, 1938-1949.
11. G. Fang, C. Zhu, M. Chen, J. Zhou, B. Tang, X. Cao, X. Zheng, A. Pan and S. Liang, *Adv. Funct. Mater.*, 2019, **29**, 1808375.
12. J. Huang, Z. Guo, Y. Ma, D. Bin, Y. Wang and Y. Xia, *Small Methods*, 2019, **3**, 1800272.
13. X. Jia, C. Liu, Z. G. Neale, J. Yang and G. Cao, *Chem. Rev.*, 2020, **120**, 7795-7866.
14. Y. Shen, Z. Li, Z. Cui, K. Zhang, R. Zou, F. Yang and K. Xu, *J. Mater. Chem. A*, 2020, **8**, 21044-21052.
15. Y. Shen, K. Zhang, F. Yang, Z. Li, Z. Cui, R. Zou, Q. Liu, J. Hu and K. Xu, *Sci. China-Mater.*, 2020, **63**, 1205-1215.
16. L. Li, L. Jiang, Y. Qing, Y. Zeng, Z. Zhang, L. Xiao, X. Lu and Y. Wu, *J. Mater. Chem. A*, 2020, **8**, 565-572.
17. W. Shang, W. Yu, X. Xiao, Y. Ma, C. Cheng, Y. Dai, P. Tan and M. Ni, *Electrochim. Acta*, 2020, **353**, 136535.
18. H. Zhang, X. Zhang, H. Li, Y. Zhang, Y. Zeng, Y. Tong, P. Zhang and X. Lu, *Green Energy Environ.*, 2018, **3**, 56-62.
19. C. Xu, J. Liao, C. Yang, R. Wang, D. Wu, P. Zou, Z. Lin, B. Li, F. Kang and C.-P. Wong, *Nano Energy*, 2016, **30**, 900-908.
20. M. Gong, Y. Li, H. Zhang, B. Zhang, W. Zhou, J. Feng, H. Wang, Y. Liang, Z. Fan, J. Liu and H. Dai, *Energy Environ. Sci.*, 2014, **7**, 2025–2032.
21. X. Zhang, A. Wu, X. Wang, C. Tian, R. An and H. Fu, *J. Mater. Chem. A*, 2018, **6**, 17905-17914.
22. B. Zhang, K. Xu, X. Fu, S. Guan, X. Li and Z. Peng, *J. Alloy. Compd.*, 2021, **856**, 158094.
23. Q. Wang, Z. Liu, H. Zhao, H. Huang, H. Jiao and Y. Du, *J. Mater. Chem. A*, 2018, **6**, 18720-18727.
24. H. C. Chen, S. Jiang, B. Xu, C. Huang, Y. Hu, Y. Qin, M. He and H. Cao, *J. Mater. Chem. A*, 2019, **7**, 6241-6249.
25. J. Wen, Z. Feng, H. Liu, T. Chen, Y. Yang, S. Li, S. Sheng and G. Fang, *Appl. Surf. Sci.*, 2019, **485**, 462-467.
26. S. Yang, C. Li, Y. Wang, S. Chen, M. Cui, X. Bai, C. Zhi and H. Li, *Energy Storage Mater.*, 2020, **33**, 230-238.
27. L. Song, Q. Wang, X. Ye, F. Yang, L. Wang, Y. Wu, F. Xu and Y. Wang, *ACS Mater. Lett.*, 2021, **3**, 1016-1024.
28. Q. Li, Q. Zhang, Z. Zhou, W. Gong, C. Liu, Y. Feng, G. Hong and Y. Yao, *Nano Res.*, 2020, **14**, 91-99.

29. Q. Li, Y. Li, J. Zhao, S. Zhao, J. Zhou, C. Chen, K. Tao, R. Liu and L. Han, *J. Power Sources*, 2019, **430**, 51-59.
30. Z. Gao, N. Song and X. Li, *J. Mater. Chem. A*, 2015, **3**, 14833-14844.
31. W. Lu, J. Shen, P. Zhang, Y. Zhong, Y. Hu and X. Lou, *Angew. Chem., Int. Ed.,* 2019, **58**, 15441-15447.
32. J.-W. Shi, Y. Zou, L. Cheng, D. Ma, D. Sun, S. Mao, L. Sun, C. He and Z. Wang, *Chem. Eng. J.*, 2019, **378**, 122161.
33. J. Sun, H. Xue, N. Guo, T. Song, Y. R. Hao, J. Sun, J. Zhang and Q. Wang, *Angew. Chem., Int. Ed.*, 2021., **60**, 19435-19441.
34. F. Yang, Y. Shen, Z, Cen, J. Wan, S. Li, G. He, J. Hu and K. Xu, *Sci. China-Mater.*, 2021, doi: 10.1007/s40843-021-1739-0.
35. H. Chen, Z. Shen, Z. Pan, Z. Kou, X. Liu, H. Zhang, Q. Gu, C. Guan and J. Wang, *Adv. Sci.*, 2019, **6**, 1802002.
36. X. Xue, J. Zhong, J. Liu, Z. Hou, X. Wu, S. Li and M. Yu, *J. Energy Storage*, 2020, **31**, 101649.
37. L. Wang, D. Jia, L. Yue, K. Zheng, A. Zhang, Q. Jia and J. Liu, *ACS Appl. Mater. Interfaces*, 2020, **12**, 47526-47538.
38. C. Yu, Z. Liu, X. Han, H. Huang, C. Zhao, J. Yang and J. Qiu, *Carbon*, 2016, **110**, 1-7.
39. Q. Zhou, Y. Gong and K. Tao, *Electrochim. Acta*, 2019, **320**, 134582.
40. Y. Niu, M. Xiao, J. Zhu, T. Zeng, J. Li, W. Zhang, D. Su, A. Yu and Z. Chen, *J Mater. Chem. A*, 2020, **8**, 9177-9184.
41. Y. Zeng, Z. Lai, Y. Han, H. Zhang, S. Xie and X. Lu, *Adv. Mater.*, 2018, **30**, 1802396.
42. Y. Lu, J. Wang, S. Zeng, L. Zhou, W. Xu, D. Zheng, J. Liu, Y. Zeng and X. Lu, *J. Mater. Chem. A*, 2019, **7**, 21678-21683.
43. S.-W. Zhang, B.-S. Yin, Y.-Z. Luo, L. Shen, B.-S. Tang, Z. Kou, X. Liu, D.-B.-K. Lim, D.-M. Gu, Z.-B. Wang and H. Gong, *Nano Energy*, 2020, **68**, 104314.
44. L. Zhou, X. Zhang, D. Zheng, W. Xu, J. Liu and X. Lu, *J. Mater. Chem. A*, 2019, **7**, 10629-10635.
45. C. Han, T. Zhang, J. Li, B. Li and Z. Lin, *Nano Energy*, 2020, **77**, 105165.
46. L. Jiang, L. Li, S. Luo, H. Xu, L. Xia, H. Wang, X. Liu, Y. Wu and Y. Qing, *Nanoscale*, 2020, **12**, 14651-14660.
47. S. Wang, S. Lai, P. Li, T. Gao, K. Sun, X. Ding, T. Xie, C. Wu, X. Li, Y. Kuang, W. Liu, W. Yang and X. Sun, *J. Power Sources*, 2019, **436**, 226867.
48. M. Li, J. Meng, Q. Li, M. Huang, X. Liu, K. A. Owusu, Z. Liu and L. Mai, *Adv. Funct. Mater.*, 2018, **28**, 1802016.
49. W. Shi, J. Mao, X. Xu, W. Liu, L. Zhang, X. Cao and X. Lu, *J. Mater. Chem. A*, 2019, **7**, 15654-15661.
50. L. Zhu, B. Fei, Y. Xie, D. Cai, Q. Chen and H. Zhan, *ACS Appl. Mater. Interfaces*, 2021, **13**, 22304-22313.
51. W. Zhou, D. Zhu, J. He, J. Li, H. Chen, Y. Chen and D. Chao, *Energy Environ. Sci.*, 2020, **13**, 4157-4167.